Modelling Silicon Photomultipliers For the Direct Detection of Dark Matter - Final Report

1713620

Department of Physics, University of Warwick, Coventry CV4 7AL, United Kingdom

12/03/2020

The direct detection of dark matter has still not been achieved. Many attempts are underway including the global DarkSide-20k collaboration. The light-sensing technology (SiPMs) used in this experiment will be tested at Warwick. This paper documents the building of model circuits in Multisim which constitute a toolkit for investigation of this technology. The typical SiPM output was simulated in order to prepare for the testing process. The simulation was realistic and could be effectively analysed. The results of this work will prove useful for the testing process, the realisation of the DarkSide-20k experiment, and will provide tools for wider research.

I. Introduction

One of the latest endeavours in the direct detection of dark matter is DarkSide-20k. So-called as it will use 20 thousand kilograms of detector material. This global collaboration aims to detect WIMP dark matter through the use of a liquid Argon detector. The detector relies on the production of a light signal. The light sensors used in this detector will be Silicon photomultipliers (SiPMs). SiPMs have not been used in a detector such as this before. They offer numerous benefits over the current technology - photomultiplier tubes (PMTs).

This document details a project which had the aim of developing a computer-based model of a SiPM and using this to create analysis software. This software will be used to test and characterise the SiPMs before they go into the DarkSide-20k detector. This process occurred in three stages. Firstly, a series of model circuits were built which output a SiPM signal. Secondly, a Monte Carlo method was used to simulate different types of noise that occur in SiPM signals before finally writing software to analyse it.

This paper will outline the concepts behind dark matter detection and SiPMs before moving on to describe the work that was undertaken.

A. Evidence For Dark Matter

Despite its existence first being proposed in 1932, dark matter didn't come into the fore until the 1980s. Jan Oort (1932) and Fritz Zwicky (1933) were the first to spot that galaxies seem to have a stronger gravitational pull than their luminous masses would suggest [1, 2]. Since then, studies of the rotation velocities of galaxies, gravitational lensing and other phenomena have provided a plethora of indirect evidence for some undetected mass in the universe - dark matter [3, 4, 5, 6, 7]. It is estimated that 83.8% of all matter is dark [8], yet direct detection remains elusive. The relative proportions of the different mass and energy components of the universe are shown in Figure 1.

Dark matter has (thus far) only been observed through its gravitational effects. Therefore, it follows naturally that dark matter cannot (or can only very rarely) interact with normal baryonic matter. The question of what this invisible mass is composed of remains one of the greatest challenges of modern physics. Many theories have been proposed, but there is still no solution to the problem. Dark matter cannot be directly studied yet so, to build a testable model, grand assumptions must be made about its composition and properties. A common assumption is that dark matter consists of particles that are yet to be directly detected. Some of the particle-nature candidates for dark matter are shown in Figure 2.

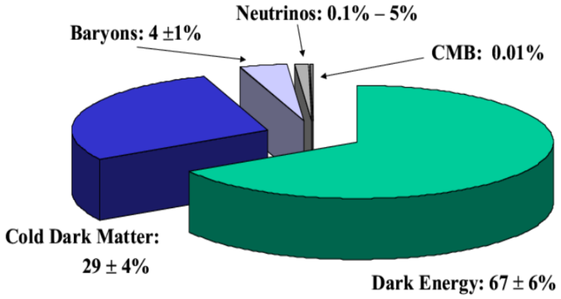

Figure 1: The relative abundances of the different constituents of the universe. Over 95% of the universe is made up of dark matter and dark energy [9].

An early explanation for the observed gravitational discrepancies were dim stars, stellar remnants and primordial black holes (PBHs) [10]. Studies have since shown that these objects could only make up a minute proportion of dark matter [11, 12, 13].

B. The WIMP Model

It is now known that dark matter consists of non-baryonic material. The two most popular candidates for dark matter particles are axions and weakly interacting massive particles (WIMPs). Both of these had already been proposed in particle physics,

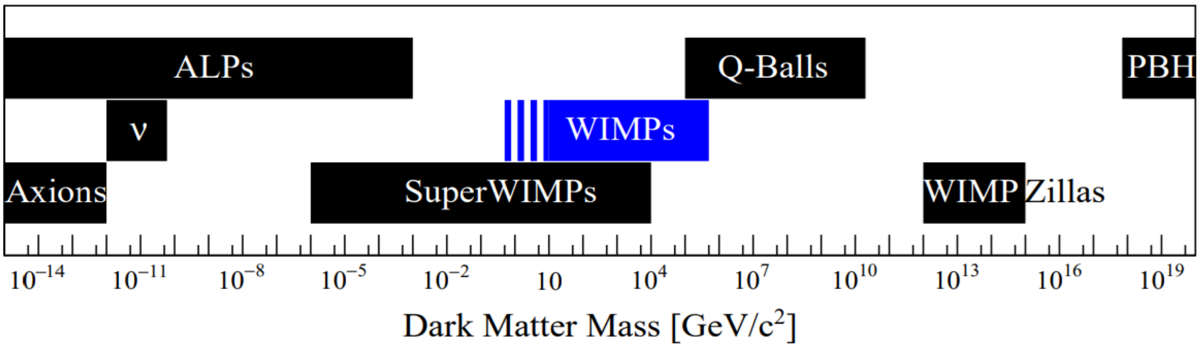

Figure 2: The different dark matter candidates and their predicted mass ranges. WIMPs (the focus of the DarkSide-20k project) are highlighted in blue [8].

independent from the search for dark matter. The focus of this paper is on WIMPs so axions will not be discussed here. The motivations for and theory behind axions can be found in [14].

WIMPs have been proposed in theories going beyond the standard model. They are defined as massive, electrically neutral particles which only interact through the weak force. It is assumed that WIMPs were thermally produced in the early universe and annihilate with each other. Taking into account that they must have cross-sections on the scale of the weak force, the number of WIMPs remaining in the universe today can be estimated. The result states that WIMPs should make up approximately 25% of all matter and energy in the universe - just below the observed abundance of dark matter (see Figure 1). This coincidence is known as the “WIMP miracle” and makes this particle one of the frontrunners in the search for dark matter [8, 10].

C. WIMP Detection and Detector Types

Due to their non-interactive nature, WIMPs have not yet been detected. There are four ways in which the search for WIMPs is proceeding:

- WIMP production at CERN.
- Direct detection from scattering experiments.
- Indirect detection from dark matter annihilation products.
- The search for dark stars.

See [10] for descriptions of the particle detection attempts and see [15] for a review of dark stars. This paper will focus on direct detection from scattering experiments.

There are several different types of detector used in direct detection experiments. Fundamentally, WIMP detectors all work off the assumption that electrically neutral WIMPs will not interact with atomic electrons, but do have a very small chance of colliding elastically with atomic nuclei. This collision would produce a detectable energy transfer. The summary below largely follows the information given in [8].

Anorganic Crystal Detectors were used in the very first experimental attempt at dark matter detection in 1987 [16]. This type of detector uses a high purity Germanium (HPGe) crystal as a target. For a semiconductor such as this, only a small amount of energy is required to form an electron-hole pair. A dark matter interaction should be easily detectable as many signal carriers will be produced in the event. The biggest issues with this detector are scalability and the lack of shielding to background radiation. Germanium crystal becomes very costly as the size of the target increases. This prevents making massive detectors of this kind which, given the rarity of dark matter interactions, significantly reduces the chances of a successful detection.

Cryogenic Detectors operate at temperatures of less than 50mK. They use dielectric crystalline targets such as Ge or Si. The system is weakly coupled to a heat bath and, upon interaction, two signals are measured simultaneously: a phonon signal and an ionisation signal. However, operation at such low temperatures makes these detectors very expensive and limited in size.

Bubble Chambers maintain superheated liquids at a temperature just below their boiling point. A dark matter interaction will cause a phase change in the liquid and a microscopic bubble of gas will form. A common problem with WIMP detection is the challenge of distinguishing nuclear recoil from electronic recoil which both produce similar signals. Electronic recoil can be caused by background γ or β radiation. For a bubble to be formed, the energy deposited within a given length $\left(\frac{dE}{dx}\right)$ must exceed a critical value which varies with the temperature of the liquid. The amount of energy that an incident particle imparts onto the liquid depends on its stopping power. Thus, different particle interactions produce different ionisation densities which provides a means to discriminate between different particles. [17] Therefore, the experiment can be tuned so that bubbles can only be formed through interactions with neutrons, α particles or WIMPs. This eliminates the possibility of eletronic recoil creating bubbles. If the background radiation can be significantly reduced, neutrons and α particles would not be present in the detector. Therefore, the only remaining cause of bubble formation is WIMP interaction, meaning WIMPs can be unambiguously detected. One major benefit of bubble chambers is that they can achieve target masses of around 50kg, making them one of the leading prospects in dark matter detection.

Noble Liquid Detectors use liquid Argon or

Xenon as the target material. A diagram of this kind of detector is shown in Figure 3. Argon and Xenon are easily ionised. In the event of a WIMP collision, ions, X^+, and excited atoms, X^*, are produced. The excited atoms combine with neutral atoms to form excimer states, X_2^*, which then decay, giving off scintillation light. An electric field, a "drift field", is applied across the detector fluid to pull ions and ionised electrons apart to prevent them from recombining. In order to distinguish electronic recoil from nuclear recoil, two signals (S1 and S2) are measured. Both of these signals are detected by photosensors, traditionally photomultiplier tubes (PMTs). The ionised electrons provide the second signal. To produce the S2 signal, a gas phase is positioned at the top of the detector. When the electrons arrive at the phase boundary, they are pulled across the gas phase by a strong "extraction field". They then produce a signal proportional to the number of electrons extracted. In electronic recoil, the number of ionised electrons is much greater than in nuclear recoil. Thus, a weaker S2 signal is expected for nuclear recoil. The ratio of S2/S1 can therefore distinguish between the two types of interaction.

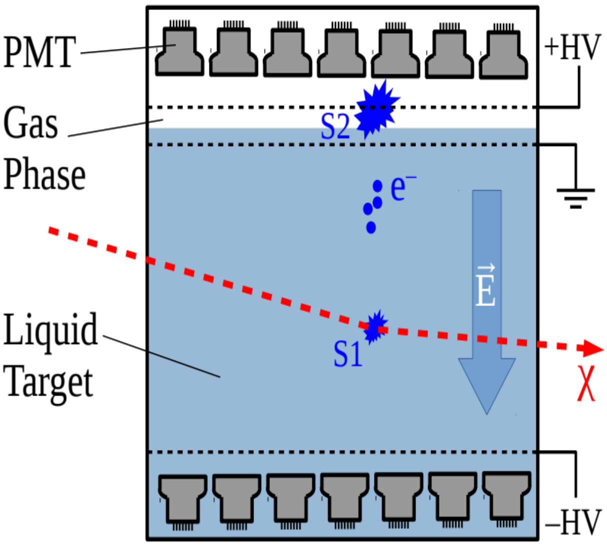

Figure 3: The photomultiplier tubes (PMTs) first detect the scintillation signal (S1). The two electric fields then extract the electrons for the detection of the second signal (S2). [8]

D. The DarkSide-20k Experiment

One upcoming attempt at directly detecting WIMPs comes in the form of the DarkSide-20k project. The experiment will run for a minimum of 5 years and aims to finally detect WIMP dark matter. It will use a Noble Liquid Detector with Liquid Argon (LAr) as the target material inside a Time Projection Chamber (TPC).

As has been discussed, this type of detector can distinguish between nuclear and electronic recoil. Therefore, background γ and β radiation is not of much concern. The most dangerous type of background radiation for this experiment is from neutrons. Single neutron-nucleus interactions produce identical signals to WIMP-nucleus interactions. Shielding provides protection against neutrons entering the TPC from the external environment. However, the components within the TPC may emit radiogenic neutrons which cannot be shielded against. Neutron induced recoils such as this are suppressed by a liquid-scintillator neutron veto (LSV). This is a separate detector surrounding the TPC which detects internal and external neutrons. This allows recoils from these neutrons to be identified and rejected. The LSV is surrounded by a Cherenkov detector called a Water Cherenkov Veto (WCV). This provides additional stopping power for external neutrons and γ radiation, as well as lowering the energy threshold for neutron detection in the LSV. Furthermore, the materials used in the detector are carefully chosen to reduce radiogenic neutrons as much as possible [18, 19].

E. Photomultiplier Tubes and Silicon Photomultipliers

In the past, Noble Liquid Detectors have used photomultiplier tubes (PMTs) to detect the 2 signals given off by the target material [20, 21, 22, 23]. PMTs take advantage of the photoelectric effect and electron multiplication. A diagram of a PMT is shown in Figure 4. A photon strikes a surface with a low work function (a photocathode) and an electron is emitted. The electron is accelerated to a second surface where the impact causes the emission of *several* electrons. This process is repeated so that many electrons are available for signal detection [24].

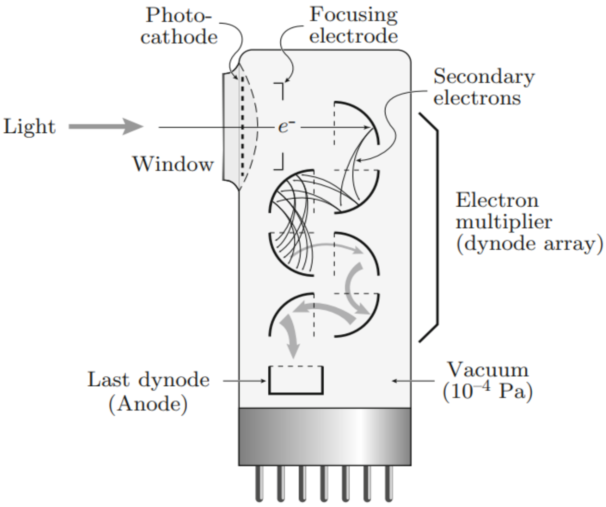

Figure 4: A photon passes through a window and begins the process of electron multiplication. The electrons then provide a signal which indicates the incidence of the photon. [24]

The DarkSide-20k project will use a similar, but more advanced technology: Silicon Photomultipliers (SiPMs). These offer greater photon detection efficiency than PMTs, better single-photon resolution, and lower electrical power requirements. Furthermore, a key component of PMTs is glass which produces radiogenic neutrons. SiPMs contain no glass, making them a much better choice of photosensor for this project as they help to keep background radiation to a minimum.

The following discussion of SiPMs uses information given in [25]. The fundamental technology at the heart of the SiPM is the avalanche photodiode (APD). The APDs are designed to work in Geiger-mode, meaning they are capable of detecting single-photons. An APD consists of a photodiode, a resistor and (although not

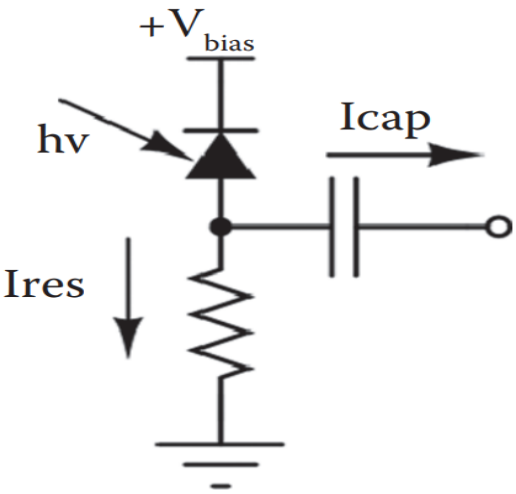

Figure 5: Circuit diagram of a Geiger-mode APD. A photon (shown as hv) strikes the photodiode and current begins to flow down two paths: I_{res} and I_{cap}. [25]

always) a capacitor as shown in Figure 5. The breakdown voltage of a photodiode is the point at which the reverse bias is broken and current flow rapidly increases. In order to operate in Geiger-mode, a bias voltage, V_{bias}, must be applied which is greater than the breakdown voltage, V_{br}. Initially, even with the application of V_{bias}, there is no current flow in the photodiode. Upon the incidence of a photon, an electron-hole pair is created. The electron is accelerated by V_{bias} and additional electrons undergo impact ionisation, causing avalanche multiplication. Now that the current is flowing, the voltage increases across the resistor. Across the photodiode the voltage now drops below V_{br}. This allows the directional bias of the photodiode to recover and stop the current flow. With no current, the voltage across the resistor drops back down again. Finally, the voltage across the photodiode rises back up to V_{bias}, making the system ready to detect the next photon.

There are two key limitations of an individual APD. Firstly, an APD is incapable of detecting how many photons are incident on the photodiode at one time. Secondly, the area of the photodiode is limited in size, for two reasons:

- Thermal noise in the diode increases with active area (the area capable of detecting photons).

- A larger active area increases the capacitance of the APD, and a greater capacitance increases its recovery time (the time that the APD is insensitive to incoming photons).

To work around these limitations, a SiPM is made up of many APDs (hundreds or thousands per square millimetre). In a SiPM, each APD is called a microcell. Figure 6 shows an array of microcells forming a SiPM.

A SiPM allows for the detection of multiple photons (as shown in Figure 7). The need for small-area photodiodes, as well as resistor and capacitor elements, means there is dead space in each microcell. This limits the total active area. The percentage of the total area that is active is called the fill factor. A higher fill factor allows for greater photon detection efficiency (PDE) - a key parameter of SiPMs.

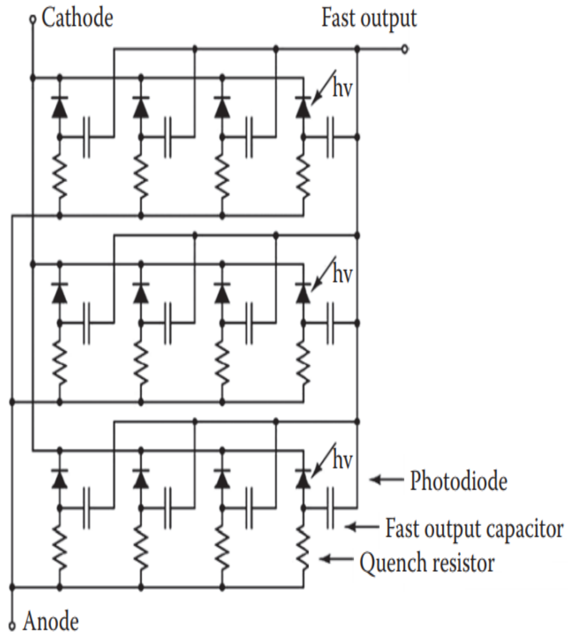

Figure 6: A SiPM made up of a 4x3 array of parallel-connected microcells. The bias voltage is applied across the cathode and the anode. [25]

Other parameters are:

Gain - the internal gain of the SiPM in response to a single-photon interaction.

Dark Count Rate - the number of false signals measured per second due to thermal noise. Dark count signals have the same amplitude as single-photon pulses. (See Figure 7.)

Crosstalk - The output signal caused by one microcell randomly firing one or more additional microcells in the array. (See Figure 7.)

Afterpulsing - Secondary avalanche events that are caused by trapped charge carriers from a previous avalanche event.

Dynamic Range - The ability of a SiPM to detect incoming photons without saturation.

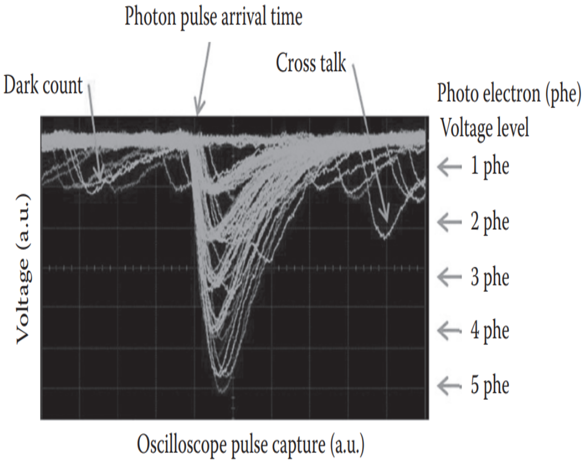

Figure 7: An oscilloscope reading of a SiPM signal after low-level light pulse. The ability of the SiPM to detect multiple photons is shown by the 5 discrete voltage levels which represent the detection of 1 photon to 5 photons [25].

F. Crosstalk and Afterpulsing Probability

Photon-detection and dark counts are known as primary events. When a microcell is triggered due to a primary event, it has the potential to generate secondary events (crosstalk and afterpulsing).

Crosstalk occurs from a primary event when the primary microcell simultaneously triggers one or more of those immediately next to it. Microcells triggered via crosstalk are capable of producing further crosstalk events in additional microcells. Thus, crosstalk is best described as a branching Poisson process, shown in Figure 8. [26]

For such a process, the probability, $P(x)$, of x events occurring is given by a generalised Poisson distribution with a shape charac-

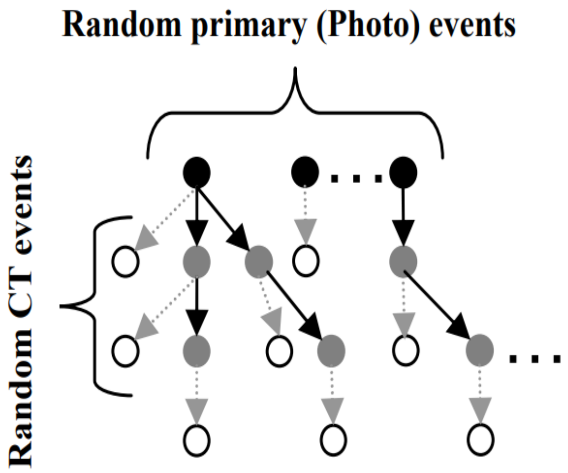

Figure 8: An initial photo event triggering a microcell which then causes a chained process of branching crosstalk in neighbouring microcells [26].

terised by the parameters θ and λ [27]:

$$P(x) = \frac{1}{x!}\theta(\theta + \lambda x)^{x-1}e^{-\theta-\lambda x} \qquad (1)$$

Figure 9 shows the shape of the generalised Poisson distribution, plotted using pyplot, for $\theta = 3.5$ and $\lambda = 0.51$. The choice for θ here is fairly arbitrary, but λ has been measured as ~ 0.51 and so was set to this value. [26]

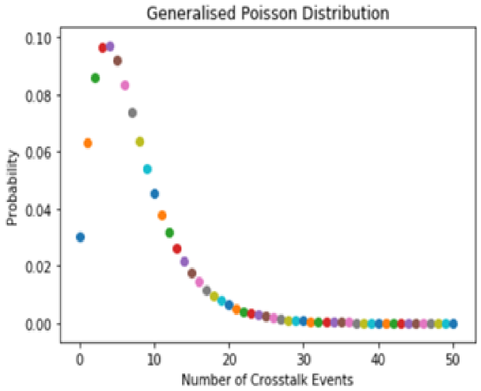

Figure 9: The shape of the generalised Poisson distribution with $\theta = 3.5$ and $\lambda = 0.51$. The probability of observing a given number of crosstalk events is plotted against the number of crosstalk events.

When a primary event occurs, the current in the microcell surges before the device self-regulates to halt the current flow. During this process, some charge carriers may become trapped in the device before discharging at a later time to produce a second pulse. This kind of event is an afterpulse and has an amplitude less than or equal to that of a primary pulse. [28] The probability of an afterpulse occurring at a given time is described by a Poisson distribution. [29] At a time, Δt, after a primary pulse, the probability, $P_{ap}(\Delta t)$ of an afterpulse taking place is given by:

$$P_{ap}(\Delta t) = \frac{1}{\tau_{ap}}e^{-\frac{\Delta t}{\tau_{ap}}} \qquad (2)$$

Where τ_{ap} is the time constant. The afterpulsing process *could* be better described using two time constants, one short and one long. However, since there is usually a time window applied for the detection of secondary events, those corresponding to the longer time constant are not detected. Thus, only one time constant is needed. The value of τ_{ap} can range from 10ns to 10μs. [29] For the Hamamatsu SiPM, τ_{ap} has been measured to be $\sim$ 15ns. [30] The shape of the afterpulsing probability distribution for $\tau_{ap} = 15$ns is shown in Figure 10.

When analysing the signal from a SiPM, the different noise types can be distinguished by plotting the amplitude of each pulse against the time since the one that preceded it. [28] An example of this is

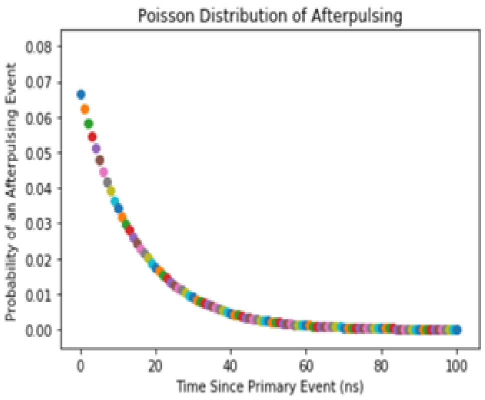

Figure 10: The probability of an afterpulse occurring is plotted against the time since the original primary event with $\tau_{ap} = 15$ns.

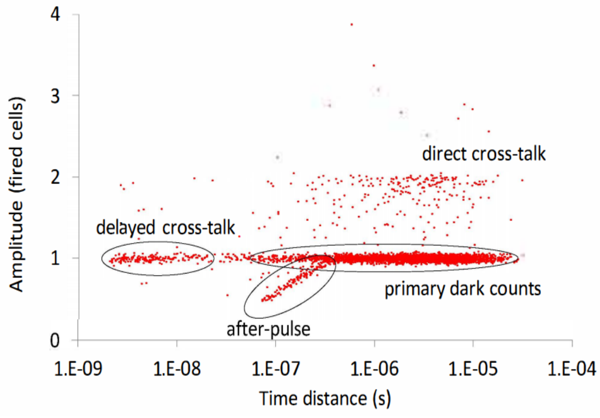

Figure 11: The different SiPM noise types appear in different areas on a plot of amplitude vs time since preceding pulse. [28]

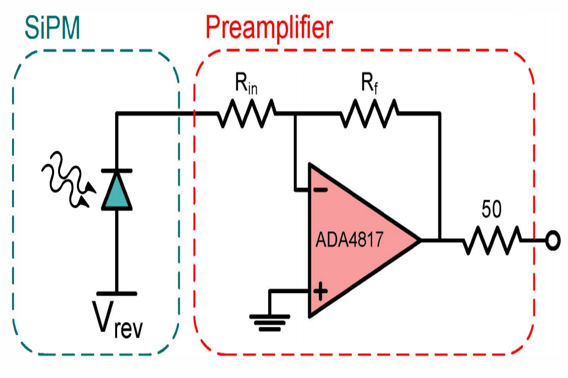

Figure 12: The model of a SiPM circuit used as a basis for the first stage of this project. [28]

shown in Figure 11. There are several important features visible in this plot. Firstly, dark counts make up a thick horizontal line with an amplitude of 1.0.

Afterpulses are visible with amplitudes in the range of 0.5 to 1.0 occurring at times of 50 to 200ns. The reason for this amplitude range is that a minimum amplitude of 0.5 was required for detection.

Finally, direct crosstalk can be seen above the dark count line, and delayed crosstalk can be seen to the left of it.

This plot from [28] demonstrates how the different noise types in a SiPM can be distinguished from each other, thus enabling characterisation of the device.

II. Methods

A. Circuit Design

The first stage of this project was to build a model of a SiPM in circuit simulation software. The software used was Multisim. The fundamental circuit design (shown in Figure 12) was based off of the one given in [28]. The design includes a SiPM (an array of microcells as in Figure 6) connected to an operational amplifier (op-amp). An oscilloscope is used to read the output of the circuit. There are two reasons for the use of the op-amp. The first is to match the impedances of the SiPM circuit and the oscilloscope to prevent signal loss. Secondly, the op-amp translates the current signal from the SiPM to voltage which can be read on the oscilloscope. From this basis, the model was further developed to match the specifications of three different SiPMs: SensL C-Series, Hamamatsu, and FBK NUV. The specifications for the SensL C-Series and Hamamatsu SiPMs are given in [31]. Those for the FBK NUV SiPM were given in [18].

B. Modelling a SiPM Pulse

Despite this project being in three distinct stages, only the first was expected to be completed. The second stage of this project was developing a program which could realistically simulate a signal from a SiPM with all the additional noise types (dark counts, crosstalk, and afterpulsing). The first step was to input a pulse shape which replicated that of a SiPM. Mathematically, this shape can be described by a function with three time constants τ_r, τ_s, and τ_l. [32, 33] (Here, r, s, and l stand for rise, short, and long respectively.) The voltage output, V, of the SiPM as a function of time, t, is shown below:

$$V(t) = \alpha\left[e^{\left(-\frac{t-t_0}{\tau_r}\right)} - e^{\left(-\frac{t-t_0}{\tau_s}\right)} - e^{\left(-\frac{t-t_0}{\tau_l}\right)}\right] \quad (3)$$

Where t_0 is the onset (i.e. the start time of the pulse) and α is a scaling factor which allows for control of the magnitude of the pulse. Using this equation, a primary pulse representing a photo event can be created which always has the same onset and amplitude. Noise can then occur from (or randomly after) this pulse. When programming the pulse function, t_0 was set to 50ns and α was set to 10. The three time constants, τ_r, τ_s, and τ_l were set to 1ns, 6ns, and 150ns respectively

C. Modelling Dark Count

The first noise type added to the signal was dark count. The number of dark count events in a given time window follows a Poisson distribution. [31] The mean value of this distribution is given by the product of the size of the time window and dark count rate (DCR). Thus, the amount of dark count can be adjusted via a DCR parameter. This parameter is set to a typical value 0.002 which corresponds to a DCR of 2MHz.

In the simulation, dark counts occur independently of the original pulse and the number observed in a given time-frame is chosen from the Poisson distribution.

D. Modelling Crosstalk

The probability distribution given in Equation (1) was used to simulate crosstalk pulses. The value of λ for crosstalk has been measured to be ~ 0.51. [26] This distribution was programmed such that the two parameters, θ and λ could be altered. The value of λ was set to 0.51. An appropriate initial value of θ was deemed to be the value that would give the probability of having no crosstalk as 0.5. Using

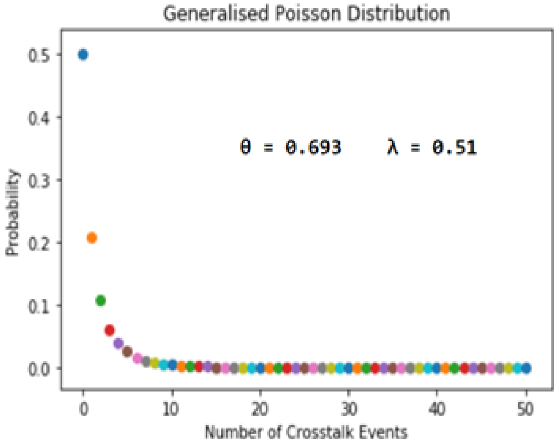

Figure 13: The probability distribution of crosstalk with $\theta = \ln(2) \simeq 0.693$ and $\lambda = 0.51$.

Equation (1) and setting $\lambda = 0.51$, $x = 0$, and $P(x) = 0.5$ it can be calculated that $\theta = \ln(2) \simeq 0.693$. The output of this function is shown in Figure 13. The next step was to program a function which would extract a random number from this distribution. To verify the accuracy of this function, a million random choices were carried out. The shape of the distribution was reproduced by these choices which confirmed the function was accurate (see Figure 14). This was then incorporated into the program.

When running through a simulation, at each primary event, a random number of crosstalk events is chosen to occur from the *generalised* Poisson distribution. The time at which these occur after the preceding primary pulse is then chosen from a Poisson distribution with a mean of 50ns (an appropriate value for crosstalk [28, 34]). A pulse with amplitude proportional to the number of crosstalk events is produced in the signal output. The maximum number of crosstalk events is set at 5.

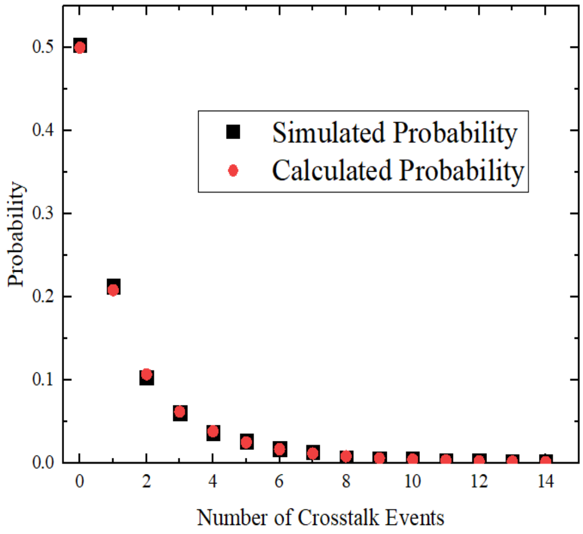

Figure 14: The shapes of both the calculated probability distribution and the distribution built up from a million random choices.

E. Modelling Afterpulsing

Afterpulsing requires the trapping of charge carriers from a primary pulse. The number of carriers trapped follows a Poisson distribution, [30], and the time at which they discharge also follows a Poisson distribution as given in Equation 2 [29]. The simulation of afterpulsing occurs in two steps. Firstly, for each primary (photo or dark) event, a number of trapped charge carriers is chosen from a Poisson distribution with a mean of 1. If this number is zero, no afterpulse occurs. If it is non-zero, then the afterpulse occurs at a time chosen from the Poisson distribution in Equation 2 (with a time constant of $\tau_{ap} = 500$ns).

In reality, the amplitude of an afterpulse is less than or equal to that of a primary

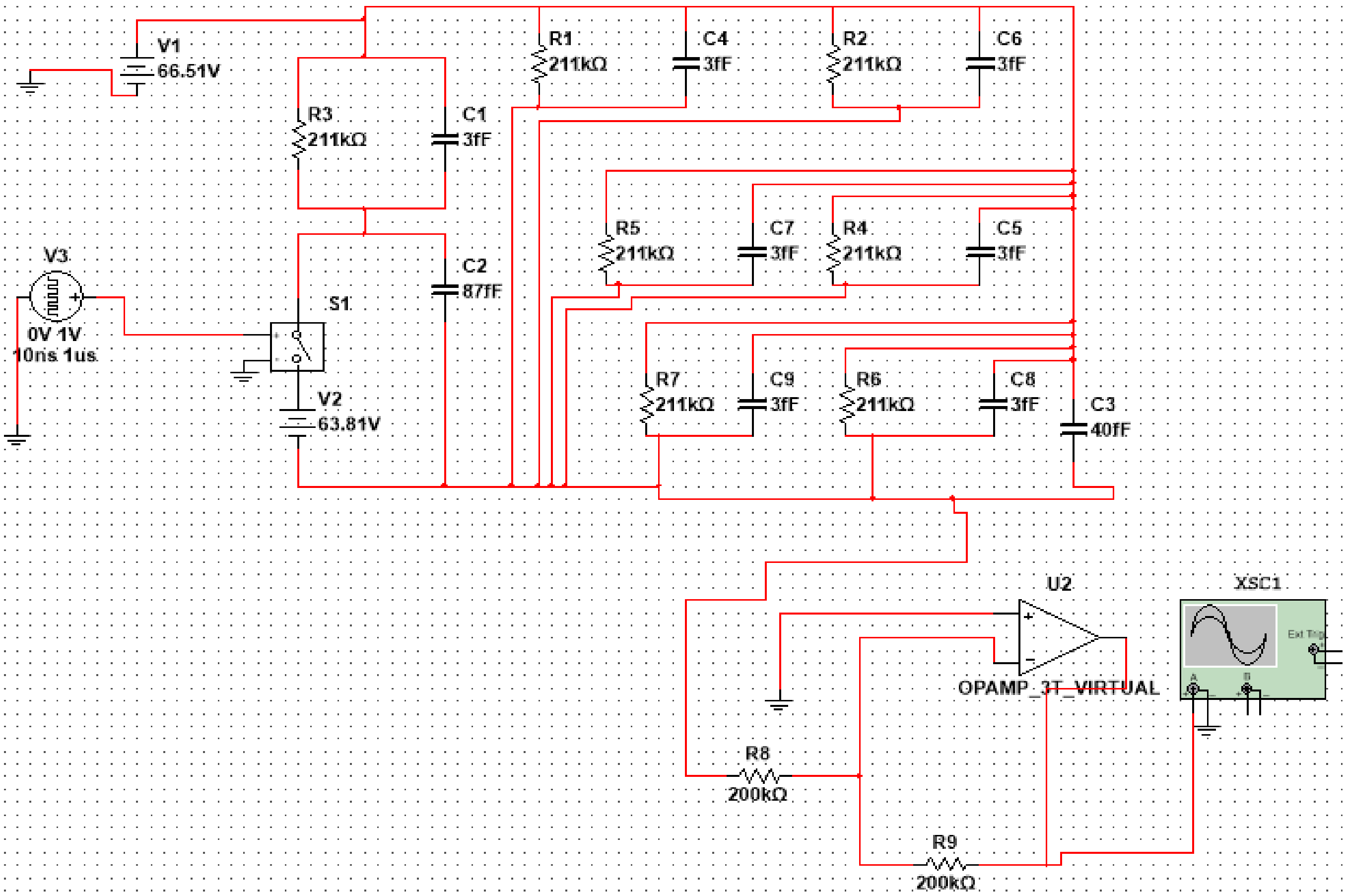

Figure 15: The circuit model of the Hamamatsu SiPM. An array of microcells is connected to an op-amp with the signal being read through an oscilloscope.

Circuit	Quench Resistance (kΩ)	Microcell Capacitance (fF)	Feedback Resistance (kΩ)
Hamamatsu	211	3	200
SensL C-Series	633	3	200
FBK NUV	2000	40	1

Table 1: The strengths of the microcell resistor (quench resistor), the microcell capacitance and the feedback resistance are displayed for each model circuit. [18, 31]

pulse. [28] However, for this simulation, the afterpulsing amplitude was chosen to be half a primary pulse so that they could be easily distinguished from dark counts.

The application of these models to the SiPM output results in a complex signal that can be used to develop software which can accurately and efficiently analyse such pulses.

III. Results

A. Building a Model SiPM Circuit

Three different models of SiPMs were built. These models were based on the SensL C-Series, Hamamatsu, and FBK SiPMs. Each model has the same structure, differing only in the resistances and capacitances of the components. The model of

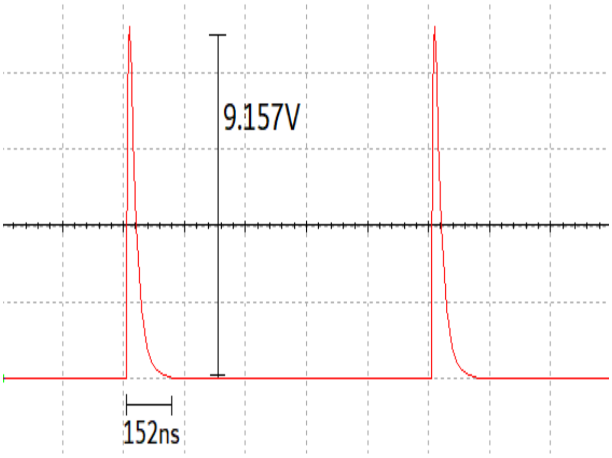

Figure 16: The output of the Hamamatsu SiPM circuit. The pulse has a peak voltage of 9.157V and it takes 152ns to recover to its original value.

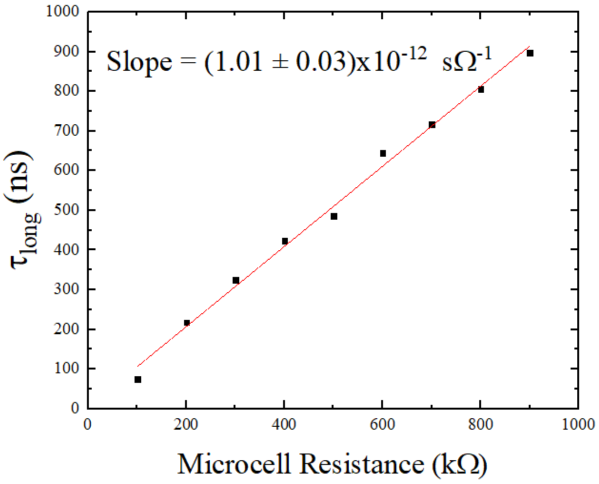

Figure 17: Microcell resistance is plotted against the value of τ_l and a linear relationship is found.

the Hamamatsu SiPM is shown in Figure 15 and its output in Figure 16. Each circuit has four distinct sections. Firstly, there is the pulse generator (left-hand side of Figure 15, labelled 'V3') which produces a square-wave of 1V amplitude with a period of 1μs (replicating a photon detection every microsecond). This signal is then fed into an array of 8 microcells. This constitutes the SiPM part of the circuit which restricts the current flow, producing a pulse signal. The third section of this circuit is a transimpedance amplifier with a 200kΩ feedback resistor. The amplifier translates the incoming current into voltage so that it can be read on an oscilloscope (the final component). The different properties of each circuit model are given in Table 1. These models have not been built simply to verify that this circuit accurately produces realistic SiPM pulses. They are effectively a toolkit with which the factors affecting the properties of a SiPM can be investigated. The components of the circuit can be altered as desired to probe the system's behaviour. This is demonstrated by altering the values of all the microcell resistors in the Hamamatsu model and observing the effect this had on the time constant τ_l. The oscilloscope data from Multisim was input into a program where a curve-fitting function fit the data to the model in Equation 3. This function then output the fit parameters such as τ_l. The resistances were changed from 100kΩ to 900kΩ. Figure 17 shows the linear relationship between these two parameters.

B. Simulating a SiPM Signal

Using the models for SiPM noise previously given, a realistic simulation of a SiPM was developed. Three noise types (in addition to some thermal noise) were added to the pure output from the circuit. These were dark count, crosstalk, and afterpulsing.

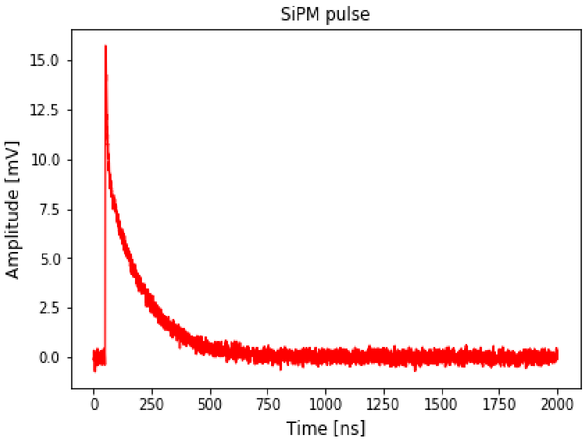

Figure 18: The output of the simulation with only thermal noise applied to the original photo pulse.

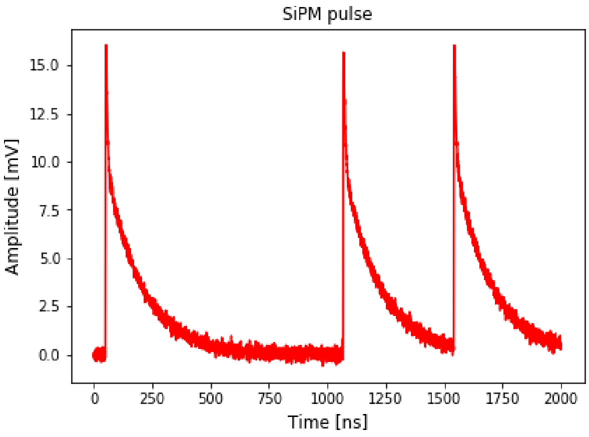

Figure 19: A signal with the original photo pulse as well as two dark pulses, one at 1068ns and the other at 1542ns.

The shape of the signal with no complex noise is shown in Figure 18. The model for dark count was added and an example of the resultant signal is given in Figure 19. Next, the crosstalk was added which produced signals such as that in Figure 20. The final simulation of the signal with dark counts, crosstalk, and afterpulsing is shown in Figure 21.

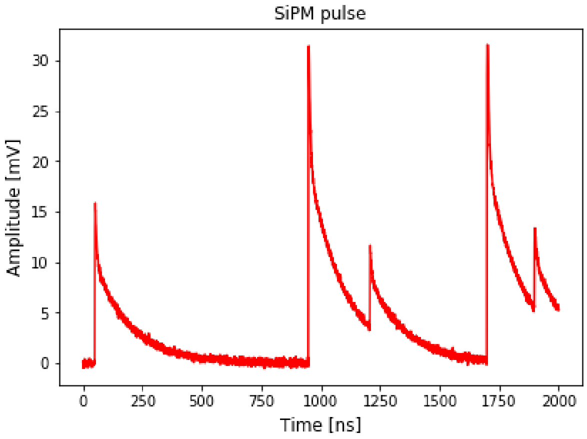

Figure 20: Two double-dark pulses occur at 948ns and 1699ns. After each of these there is a crosstalk pulse, these are at 1207ns and 1899ns.

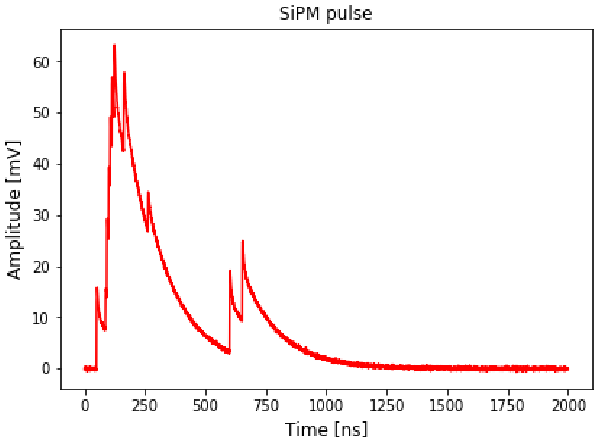

Figure 21: The full simulation of a signal from a SiPM. This includes each type of noise that can occur.

C. Signal Analysis

In order to analyse the simulated signals, a peak finder function was employed. This function detects all the peaks in a signal and returns the amplitude of each peak and its distance from the one before it. To find the best parameters for the function, a loop was programmed to run through over a million configurations. The optimal parameters were found and incorporated. The result of applying this function to a signal

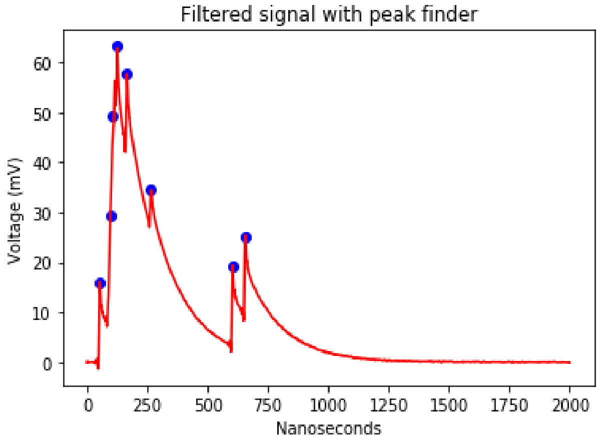

Figure 22: The result of running a peak detection program over the SiPM signal in Figure 21. It is clear that the peaks are effectively detected.

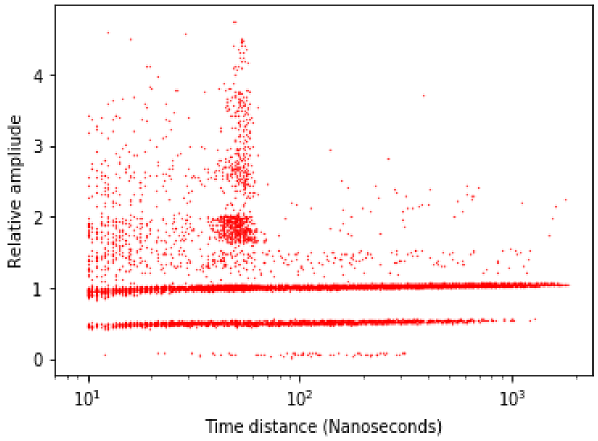

Figure 23: The amplitude of every peak from 1343 signals is plotted against the time since the peak that preceded it.

window is shown in Figure 22.

After building the peak finder, many signals could then be analysed in one go. This made it possible to build up a large amount of information about the behaviour of the SiPM model. The amplitude of each peak was plotted against its distance in time from the peak before it. The result is shown in Figure 23. The key features of this plot are:

- The horizontal line at 0.5 amplitude made up of afterpulses.
- The horizontal line at 1.0 amplitude made up of dark counts.
- A vertical bar between 40 and 60 nanoseconds which is made up of crosstalk pulses occurring at their most probable time. The number of pulses decreases as the amplitude increases since larger numbers of simultaneous events are less likely (see Figure 13).
- The diffuse scattering of points above the dark count line due to crosstalk events at less probable times.
- The thin line at ~ 0 amplitude due to anomalous detections of thermal noise.

The simulation was programmed such that the different noise types could be controlled. For example, the amount of crosstalk can be altered by changing the value of θ in Equation 1, or dark count can be varied by changing the DCR parameter. The amount of crosstalk was significantly reduced by setting $\theta = 0.2$ and the analysis program was used to make a second scatter plot. This is displayed in Figure 24 which clearly shows that the amount of crosstalk is reduced. Furthermore, the amount of afterpulsing and dark count on the plot has not changed.

Finally, a third plot (Figure 25) was made with a greatly increased crosstalk probability, but a much smaller DCR. The value of θ

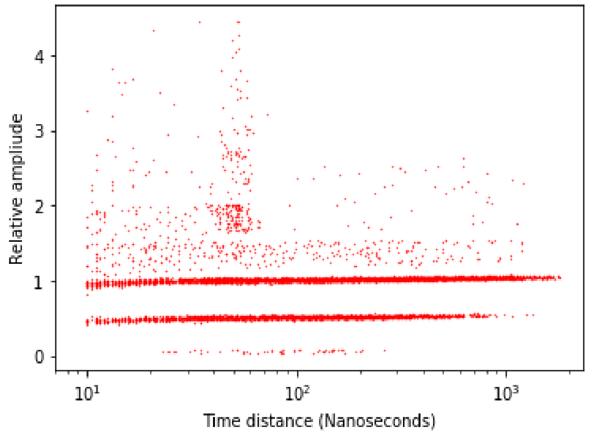

Figure 24: 1343 signals were analysed to produce a second plot. The value of θ was changed to 0.200 and the resultant reduction in crosstalk is clearly visible.

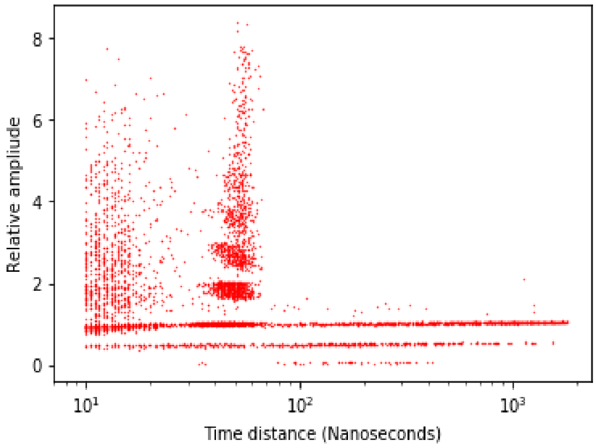

Figure 25: For the final plot, the value of θ was raised to 2 and the DCR parameter was lowered to 0.0005. The reduction in dark count and increase in crosstalk are visible.

for this data-set is 2, the maximum number of crosstalk events was increased to 10, and the DCR parameter was set to 0.0005 which corresponds to a DCR of 500kHz. Figure 25 shows the reduced dark count (and therefore also reduced afterpulsing) as well as much more crosstalk.

IV. Discussion

It is important to note that sections B, C, D, and E in Methods are actually part of the results of this project. Even though they are part of *what* was achieved, they have been included in the Methods section because they more appropriately describe *how*. In other words, the modelling and simulation of each noise type were results on their own, but they better describe how the SiPM simulation was built.

The results of this project have many potential applications both in the DarkSide-20k project and in wider researh of SiPM technology.

A. The Model SiPM Circuits

The original goal for this project was simply to build a circuit that could replicate the behaviour of a SiPM. This circuit was created, but more importantly, three different SiPM models were developed from this basis. These were models of the SensL C-Series, Hamamatsu, and the FBK NUV SiPMs. They differed only by the strengths of the resistors and capacitors in the circuits. Through alteration of these properties, the relationship between quench resistance and τ_l was found. The models with lower quench resistance have a shorter recovery time. This demonstrates how these models make up a toolkit for further investigation into how circuit properties affect the behaviour of a SiPM. Thus, what has been produced in this project has the potential to aid the development of more efficient SiPMs in the future. In spite of this, the curve-fitting function used to evaluate τ_l was not able to reliably calculate values for τ_r and τ_s. The rise times of the pulses can be in the order of picoseconds. [34] Therefore, it is likely that the surge of current during a primary event happens too quickly for the program to accurately detect. This means the data which encodes the information about τ_r is not precisely recorded, preventing τ_r from being accurately calculated.

B. SiPM Output Simulation

A simulation was created of a SiPM signal output with the original photo pulse and all the noise that can stem from or accompany it. This simulation is not only a realistic representation of a SiPM signal but it is also controllable. The levels of each type of noise can be raised or lowered by altering the parameters of the governing equations. Despite being a reasonable output from a SiPM, the simulation isn't without its flaws. Firstly, the afterpulsing is simplified. It has been previously shown that the amplitude of an afterpulse increases with the amount of time since the pulse that produced it (see Figure 11). [28, 34] In this simulation however, all afterpulses have an amplitude of 0.5. Furthermore, the distribution of crosstalk in time does not agree with that in [28] or [34]. As has been demonstrated in this paper, this simulation provides the basis from which software can be designed to analyse the simulated output and, by extension, the output from any real SiPM.

C. Signal Analysis

The signal analysis software relies on a peak finder function. It is possible that this function will not resolve two or more separate peaks if they are too close together. The efficiency of this function is calculated as the number of peaks detected divided by the total number of events that occurred. The value was estimated by collecting data from 200 SiPM signal simulations. When multiple crosstalk events occur, they happen simultaneously. This means multiple events are read by the peakfinder as only one event. When analysing SiPM signals, the number of crosstalk events is revealed by the amplitude of the peak. This makes it acceptable to merge multiple crosstalk events into one peak. However, when calculating the estimate, this results in many events being 'missed', even though this is not actually the case. Whilst there is a small number of 'extra' detections due to thermal noise, these are outweighed by the number missed due to the simultaneity of crosstalk. Therefore, this estimate provides a lower limit on the function's efficiency. It was found that the peak finder has an efficiency of at least 80.23%. The true efficiency is higher than this value, but it needs to be made more efficient for testing SiPMs. The whole purpose of this project was to prepare for the arrival of the DarkSide-20k SiPMs at Warwick, where they will undergo room-temperature testing. The signal simulation provided the foundation to build the analysis software to be used for this testing. This means that when the SiPMs arrive, their behaviour can be investigated and their properties characterised. The levels of noise from all the SiPMs can be measured so that once they go into the detector, an expected amount of noise will be known and can therefore be disregarded. These tools do not only apply to DarkSide-20k, but also apply to any attempts at SiPM characterisation.

V. Conclusions

The work performed throughout this project was done in three stages:

- Model circuits were created.
- A complex output from a SiPM was simulated.
- Software was written to analyse SiPM signals.

Model circuits were built which accurately and reliably reproduce the behaviour of existing SiPMs. These can be used for further investigation of SiPM properties and efficiency.

Three types of complex noise were simulated: dark count, crosstalk, and afterpulsing. This produced a realistic SiPM output signal which could then be analysed. However, there were issues with this simulation which reduced its ability to provide a completely accurate representation of a SiPM. A higher level of realism will aid the improvement of the analysis software as any issues that will occur with real SiPMs, will also occur with the simulation.

Analysis of this signal was performed which demonstrated how the different noise types in a SiPM can be identified during the testing process.

There are numerous opportunities for further research from this project. With more time, the curve-fitting function would be improved and made more reliable. The model circuits would also be used to extensively investigate how each component of the SiPM circuit affects its overall behaviour. Also, the simulation of the afterpulsing noise would be developed to replicate the behaviour of real SiPMs such as those studied in [28] and [34]. The ideal parameters of the afterpulsing probability equation would be found such that they produce pulses within 50 to 200ns of the preceding pulse. This would be a much more realistic time-distribution of afterpulsing. An extra level of complexity with afterpulsing, which was not included in this simulation, is the fact that the pulse amplitude scales with the time since the pulse that generated it. Further development of this work would add this complexity. If additional time was available, the efficiency of the peak finder function will be more precisely calculated. Only a lower limit could be applied in this project however, after more work, it is possible a more precise method could be developed. Finally, the analysis software developed in this project will be used to test and characterise the SiPMs for use in the DarkSide-20 collaboration.

References

[1] J. Oort, Bulletin of the Astronomical Institutes of the Netherlands **6**, 249 (1932).

[2] F. Zwicky, Helvetica Physica Acta **6**, 110 (1933).

[3] V. Rubin, W. K. Ford, and N. Thonnard, Astrophysical Journal **225**, 107 (1978).

[4] D. Clowe, M. Bradač, A. H. Gonzalez, M. Markevitch, and S. W. Randall, The Astrophysical Journal Letters **648**, 109 (2006).

[5] L. Hernquist, N. Katz, D. Weinberg, and J. Miralda-Escudé, The Astrophysical Journal **457**, 51 (1996).

[6] A. Vikhlinin, W. Forman, and C. Jones, Astrophysical Journal **474**, 7 (1997).

[7] D. Wittman, J. A. Tyson, D. Kirkman, I. Dell'Antonio, and G. Bernstein, Nature **405**, 143 (2000).

[8] M. Schumann, Journal of Physics G Nuclear and Particle Physics **46**, 103003 (2019).

[9] W. Freedman and M. S. Turner, Rev. Mod. Phys. **75**, 1433 (2003).

[10] K. Freese, International Journal of Modern Physics D **26**, 1730011 (2017).

[11] C. Alcock *et al.*, The Astrophysical Journal Letters **550**, 169 (2001).

[12] Y. Ali-Haïmoud, E. D. Kovetz, and M. Kamionkowski, Phys. Rev. D **96**, 123523 (2017).

[13] L. Wyrzykowski *et al.*, Monthly Notices of the Royal Astronomical Society **416**, 2949 (2011).

[14] D. Marsh, Physics Reports **643**, 1 (2016).

[15] K. Freese, T. Rindler-Daller, D. Spolyar, and M. Valluri, Rep. Prog. Phys. **79**, 066902 (2016).

[16] S. Ahlen *et al.*, Physics Letters B **195**, 603 (1987).

[17] F. Aubin *et al.*, New Journal of Physics **10**, 103017 (2008).

[18] C. Aalseth *et al.*, Eur. Phys. J. Plus **133**, 131 (2018).

[19] T. Undagoitia and L. Rauch, Journal of Physics G Nuclear and Particle Physics **43**, 013001 (2015).

[20] P. Agnes *et al.*, Phys. Rev Lett. **121**, 081307 (2018).

[21] M. Boulay (for the DEAP collaboration), Journal of Physics: Conference Series **375**, 012027 (2012).

[22] K. Rielage *et al.*, Physics Procedia **61**, 144 (2015).

[23] A. Marchionni *et al.*, Journal of Physics: Conference Series **308**, 012006 (2011).

[24] C. Holbrow, J. N. Lloyd, J. C. Amato, E. Galvez, and M. E. Parks, *Modern Introductory Physics: Second Edition* (Springer, New York, 1999).

[25] S. Awadalla *et al.*, *Solid-State Radiation Detectors: Technology and Applications* (CRC Press, Boca Raton, 2015).

[26] S. Vinogradov, Nuclear Instruments and Methods in Physics Research **695**, 247 (2012).

[27] P. Consul and F. Famoye, *Lagrangian Probability Distributions* (Birkhäuser, Boston, 2006).

[28] C. Piemonte *et al.*, Proc. IEEE Nucl. Sci. Symp. Med. Imag. Conf. Rec. , 428 (2012).

[29] T. Herman *et al.*, IEEE Transactions On Nuclear Science **57**, 2254 (2010).

[30] Y. Du and F. Retiére, Nuclear Instruments and Methods in Physics Research **596**, 396 (2008).

[31] P. Peng, Y. Qiang, S. Ross, and K. Burr, Nuclear Instruments and Methods in Physics Research **887**, 144 (2018).

[32] D. Tovey, *A Study of Pulse Shape Discrimination in Scintillator Dark Matter Detectors*, PhD thesis, University of Sheffield, 1998.

[33] D. Akerib *et al.*, Phys. Rev. D **97**, 112002 (2018).

[34] F. Acerbi and S. Gundacker, Nuclear Instruments and Methods in Physics Research **926**, 16 (2019).